

Valley dependent anisotropic spin splitting in silicon quantum dots

Rifat Ferdous,¹ Erika Kawakami,² Pasquale Scarlino,² Michał P. Nowak,^{2,3} D. R. Ward,⁴ D. E. Savage,⁴ M. G. Lagally,⁴ S. N. Coppersmith,⁴ Mark Friesen,⁴ Mark A. Eriksson,⁴ Lieven M. K. Vandersypen,² and Rajib Rahman¹

¹*Network for Computational Nanotechnology, Purdue University, West Lafayette, IN 47907, USA*

²*QuTech and Kavli Institute of Nanoscience, TU Delft, Lorentzweg 1, 2628 CJ Delft, The Netherlands*

³*AGH University of Science and Technology, Faculty of Physics and Applied Computer Science, al. Mickiewicza 30, 30-059 Kraków, Poland*

⁴*University of Wisconsin-Madison, Madison, Wisconsin 53706, USA*

(Dated: February 22, 2017)

Spin qubits hosted in silicon (Si) quantum dots (QD) are attractive due to their exceptionally long coherence times and compatibility with the silicon transistor platform. To achieve electrical control of spins for qubit scalability, recent experiments have utilized gradient magnetic fields from integrated micro-magnets to produce an extrinsic coupling between spin and charge, thereby electrically driving electron spin resonance (ESR). However, spins in silicon QDs experience a complex interplay between spin, charge, and valley degrees of freedom, influenced by the atomic scale details of the confining interface. Here, we report experimental observation of a valley dependent anisotropic spin splitting in a Si QD with an integrated micro-magnet and an external magnetic field. We show by atomistic calculations that the spin-orbit interaction (SOI), which is often ignored in bulk silicon, plays a major role in the measured anisotropy. Moreover, inhomogeneities such as interface steps strongly affect the spin splittings and their valley dependence. This atomic-scale understanding of the intrinsic and extrinsic factors controlling the valley dependent spin properties is a key requirement for successful manipulation of quantum information in Si QDs.

How microscopic electronic spins in solids are affected by the crystal and interfacial symmetries has been a topic of great interest over the past few decades and has found potential applications in spin-based electronics and computation^{1–7}. While the coupling between spin and orbital degrees of freedom has been extensively studied, the interplay between spin and the momentum space valley degree of freedom is a topic of recent interest. This spin-valley interaction is observed both in the exotic class of newly found two-dimensional materials^{8–10} and in silicon^{11–13} —the old friend of the electronics industry. Progress in silicon qubits in the last few years has come with the demonstrations of various types of qubits with exceptionally long coherence times, such as single spin up/down qubits^{14,15}, two-electron singlet-triplet qubits^{16,17}, three-electron exchange-only¹⁸ and hybrid spin-charge qubits^{19,20} realized in Si QDs. The presence of the valley degree of freedom has also enabled valley based qubit proposals²¹, which have potential for noise immunity. To harness the advantages of different qubit schemes, quantum gates for information encoded in different bases are required^{9,22,23}. A controlled coherent interaction between multiple degrees of freedom, like valley and spin, might offer a building block for promising hybrid systems.

Although bulk silicon has six-fold degenerate conduction band minima, in quantum wells or dots, electric fields and often in-plane strain in addition to vertical confinement results in only two low lying valley states (labeled as v_- and v_+ in Figure 1b) split by an energy gap known as the valley splitting. An interesting interplay between spin and valley degrees of freedom, which

gives rise to a valley dependent spin splitting, has been observed in recent experiments^{14,24–26}. SOI enables the control of spin resonance frequencies by gate voltage, an effect measured in refs. [15, 24]. However, the ESR frequencies and their Stark shifts were found to be different for the two valley states²⁴. In another work, an inhomogeneous magnetic field, created by integrated micro-magnets in a Si/SiGe quantum dot device, was used to electrically drive ESR¹⁴. Magnetic field gradients generated in this way act as an extrinsic spin-orbit coupling and thus can affect the ESR frequency²⁷. Remarkably, although SOI is a fundamental effect arising from the crystalline structure, the ESR frequency differences between the valley states observed in refs. [14] and [24] have different signs when the external fields are oriented in the same direction with respect to the crystal axes. To understand and achieve control over the coupled behavior between spin and valley degrees of freedom, several questions need to be addressed, such as 1) What causes the device-to-device variability?, 2) Can an artificial source of interaction, like inhomogeneous B-field, completely overpower the SOI effects of the intrinsic material?, 3) What knobs and device designs can be utilized to engineer the valley dependent spin splittings?

Here we report experimentally measured anisotropy in the ESR frequencies of the valley states f_{v_-} and f_{v_+} and their differences $f_{v_-} - f_{v_+}$, as a function of the direction of the external magnetic field (\mathbf{B}_{ext}) in a quantum dot formed at a Si/SiGe heterostructure with integrated micro-magnets. At specific angles of the external B-field, we also measure the spin splittings of the two valley states as a function of the B-field magnitude. By performing

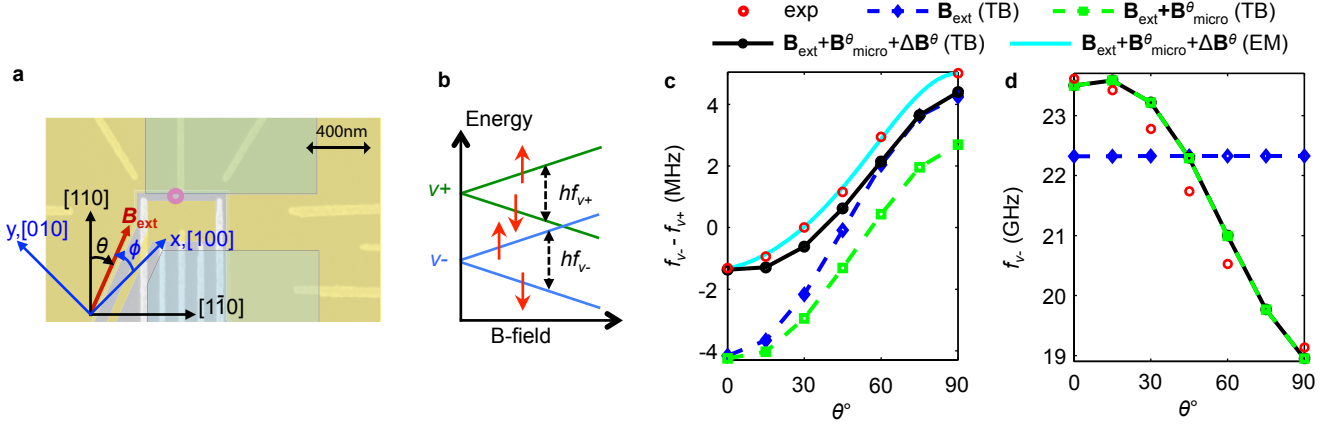


FIG. 1. **Valley dependent anisotropic ESR in a Si QD with integrated micro-magnets** **a**, False-color image of the experimental device showing the estimated location of the quantum dot (magenta colored circle) and two Co micro-magnets (green semi-transparent rectangles). The external magnetic field (\mathbf{B}_{ext}) was rotated clockwise in-plane, from the $[110]$ ($\theta = 0^\circ$) crystal orientation towards $[1\bar{1}0]$ ($\theta = 90^\circ$). **b**, Lowest energy levels of a Si QD in an external magnetic field. The valley-split levels v_- and v_+ are found to have unequal Zeeman splittings ($E_{\text{ZS}}(v_\pm) = hf_{v\pm}$), with ESR frequencies $f_{v-} \neq f_{v+}$. **c**, Both measured (red circles) and calculated $f_{v-} - f_{v+}$ as a function of θ , for $B_{\text{ext}} = 0.8$ T. The anisotropy in $f_{v-} - f_{v+}$ is governed by both internal (intrinsic SOI) and external (micro-magnetic field) factors. The anisotropy due to the intrinsic SOI, calculated from atomistic tight binding method, for a specifically chosen vertical electric field and interface step configuration, is labeled as ' \mathbf{B}_{ext} (TB)'. The micro-magnetic field is separated into a homogeneous ($\mathbf{B}_{\text{micro}}^\theta$) and an inhomogeneous ($\Delta\mathbf{B}^\theta$) part. The inclusion of $\mathbf{B}_{\text{micro}}^\theta$ in this case (labeled ' $\mathbf{B}_{\text{ext}} + \mathbf{B}_{\text{micro}}^\theta$ (TB)'), shifts the curve away from the experiment. The addition of $\Delta\mathbf{B}^\theta$ introduces additional anisotropy (labeled ' $\mathbf{B}_{\text{ext}} + \mathbf{B}_{\text{micro}}^\theta + \Delta\mathbf{B}^\theta$ (TB)') and shifts the curve towards the experiment. An effective-mass calculation, with fitted SOI and dipole coupling parameters, is also presented with a cyan solid line. **d**, Both measured (red circles) and calculated f_{v-} , as a function of θ , for $B_{\text{ext}} = 0.8$ T. Calculation with the intrinsic SOI shows negligible change in GHz scale, while the addition of $\mathbf{B}_{\text{micro}}^\theta$ results in anisotropy close to the experimental data. $\Delta\mathbf{B}^\theta$ has negligible effect on f_{v-} . Hence, the anisotropy of f_{v-} is mainly dictated by the homogeneous part of the micro-magnetic field.

spin-resolved atomistic tight binding (TB) calculations of the quantum dots confined at ideal versus non-ideal interfaces, we evaluate the contribution of the intrinsic SOI with and without the spatially varying B-fields from the micro-magnets to the spin splittings, thereby relating these quantities to the microscopic nature of the interface and elucidating how spin, orbital and valley degrees of freedom are intertwined in these devices. Finally, by combining all the effects together, we explain the experimental measurements and address the questions raised in the previous paragraph.

Fig. 1 shows the experimental device, energy levels of interest and measured anisotropic spin splittings compared with the final theoretical results. Details of the device shown in Fig. 1a can be found in ref. [14]. The external magnetic field is swept from the $[110]$ to $[1\bar{1}0]$ crystal orientation. A schematic of the energy level structure is shown in Fig. 1b depicting the v_- and v_+ valley states with different spin splittings, where v_- is defined as the ground state. In the experiment, the lowest valley-orbit excitation is well below the next excitation, justifying this four-level schematic in the energy range of interest.

The atomistic calculation with SOI alone (labeled ' \mathbf{B}_{ext} (TB)') for a QD at a specifically chosen non-ideal interface and vertical electric field (E_z) qualitatively captures the experimental trend of $f_{v-} - f_{v+}$ in Fig. 1c, but fails to reproduce the anisotropy of the measured f_{v-} in

Fig. 1d in the larger GHz scale. The differences between the experimental data and the SOI-only calculations in both figures arise from the micro-magnets present in the experiment. We can separate the contribution from the micro-magnet into two parts, a homogeneous (spatial average, $\mathbf{B}_{\text{micro}}^\theta$) and an inhomogeneous (spatially varying, $\Delta\mathbf{B}^\theta$) magnetic field. The superscript θ here indicates that the micro-magnetic fields depend on the direction of \mathbf{B}_{ext} (supplementary section S4). The inclusion of the homogeneous part of the micro-magnetic field creates an anisotropy in the total magnetic field (supplementary Fig. S7), which captures the anisotropy of f_{v-} in Fig. 1d very well ($f_{v-} \approx g\mu|\mathbf{B}_{\text{ext}} + \mathbf{B}_{\text{micro}}^\theta|/h$, where g is the Landé g-factor, μ is the Bohr magneton and h is the Planck constant), but quantitative match with the experimental data in Fig. 1c is not obtained. Next, we also incorporate the inhomogeneous part of the micro-magnetic field, and witness a close quantitative agreement in the anisotropy of $f_{v-} - f_{v+}$, while the anisotropy of f_{v-} is unaffected. This experiment-theory agreement of fig. 1c is achieved for a specific choice of interface condition and E_z , whose influence will be discussed later. Here, we conclude that mainly the intrinsic SOI and the extrinsic inhomogeneous B-field govern the anisotropy of $f_{v-} - f_{v+}$ on the MHz scale, while the anisotropy in the total homogeneous magnetic field introduced by the micro-magnet dictates the anisotropy of f_{v-} (and f_{v+}) on the larger

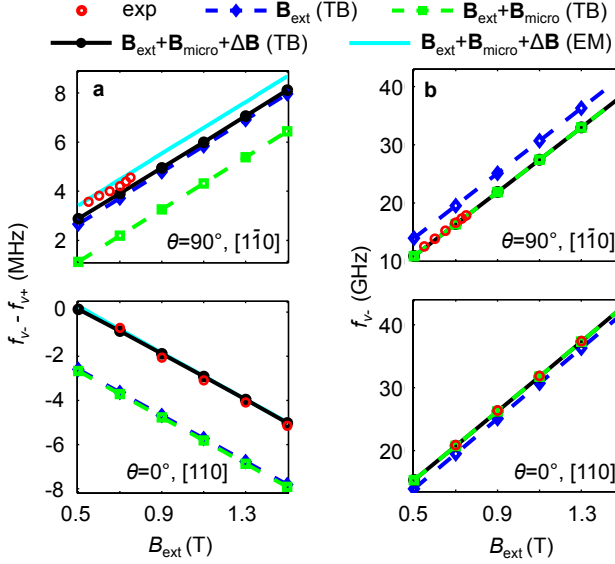


FIG. 2. Measured ESR frequencies, ($f_{v\pm}$) and their differences for the two valley states as a function of the external B-field magnitude B_{ext} along two crystal directions, and comparison with theoretical calculations. **a**, $f_{v-} - f_{v+}$ and **b**, f_{v-} with B_{ext} along $[110]$ ($\theta = 0^\circ$) (bottom panel) and $[1\bar{1}0]$ ($\theta = 90^\circ$) (top panel). As in Figs. 1c and 1d, the calculations progressively include SOI (labeled ' B_{ext} (TB)'), homogeneous ($B_{\text{ext}} + B_{\text{micro}}$ (TB)'), and gradient (labeled ' $B_{\text{ext}} + B_{\text{micro}} + \Delta B$ (TB)') B-field of the micro-magnet. The cyan solid lines are the effective mass calculations and the red circles are the experimental data. The dependence (slope) of $f_{v-} - f_{v+}$ on B_{ext} in (a) comes from the SOI, while the micro-magnetic fields provide a shift independent of B_{ext} .

GHz scale.

In Fig. 2, we show the measurements of the spin splittings as a function of the magnitude of B_{ext} (B_{ext}), together with the theoretical calculations. The bottom panels show $f_{v-} - f_{v+}$ (Fig. 2a) and f_{v-} (Fig. 2b) for B_{ext} along $[110]$ ($\theta = 0^\circ$), whereas the top panels correspond to the B-field along $[1\bar{1}0]$ ($\theta = 90^\circ$). In Fig. 2b, f_{v-} depends on B_{ext} through $g_- \mu B_{\text{tot}} / h$, with $B_{\text{tot}} = |B_{\text{ext}} + B_{\text{micro}}|$. The addition of B_{micro} causes a change in B_{tot} and shifts f_{v-} to coincide with the experimental data. The contributions of ΔB and SOI are negligible here in the GHz scale.

On the other hand, comparing the calculated $f_{v-} - f_{v+}$ from SOI alone (labeled ' B_{ext} (TB)') for the chosen E_z and interface condition, with experimental data, in both the top and bottom panels of Fig. 2a, it is clear that the experimental B-field dependence of $f_{v-} - f_{v+}$ (the slope, $\frac{d(f_{v-} - f_{v+})}{dB_{\text{ext}}}$) is captured from the effect of intrinsic SOI, except for a shift between the SOI curve and the experimental data (different shift for $\theta = 0^\circ$ and $\theta = 90^\circ$). The addition of B_{micro} alone does not result in the necessary shift to match the experiment. Only after adding ΔB can a quantitative match with the experiment be achieved.

Again the experiment-theory agreement is conditional on the interface condition and E_z . Moreover, we see that the addition of ΔB does not change the dependency on B_{ext} . Therefore, to properly explain the observed experimental behavior, we can ignore neither the SOI, which is responsible for the change in $f_{v-} - f_{v+}$ with B_{ext} , nor the inhomogeneous B-field which shifts $f_{v-} - f_{v+}$ regardless of B_{ext} .

Note that to obtain a quantitative agreement between the experiment and the atomistic TB calculations, simultaneously in the anisotropy (Fig. 1c) and the B_{ext} (Fig. 2a) dependence of $f_{v-} - f_{v+}$, the only knobs we have to adjust are 1) E_z and 2) interfacial geometry i.e. how many atomic steps at the interface lie inside the dot and where they are located relative to the dot center. These adjustments have to be done iteratively since the steps and E_z not only affect the intrinsic SOI but also the influence of the inhomogeneous B-field. It is easy to separate out the contribution of the SOI from the micro-magnet in the B_{ext} dependence of $f_{v-} - f_{v+}$. It will be shown in Figs. 3 and 4 that, the slope, $\frac{d(f_{v-} - f_{v+})}{dB_{\text{ext}}}$ originates from the SOI, while the micro-magnetic field shifts $f_{v-} - f_{v+}$ independent of B_{ext} . First we individually match the experimental "slope" from the SOI and the "shift" from the contribution of the micro-magnet for some combinations of the two knobs. Finally both effects together quantitatively match the experiment for $E_z = 6.77 \text{ MVm}^{-1}$, and an interface with four evenly spaced monoatomic steps at -24.7 nm, -2.9 nm, 18.7 nm, 40.4 nm from the dot center along the x ($[100]$) direction. This combination also predicts a valley splitting of $34.4 \mu\text{eV}$ in close agreement with the experimental value, given by $29 \mu\text{eV}$ ²⁶. To describe the QD, a 2D simple harmonic (parabolic confinement) potential was used with orbital energy splittings of 0.55 meV and 9.4 meV characterizing the x and y ($[010]$) confinement respectively. As the interface steps are parallel to y direction, the orbital energy splitting along y has negligible effects, but the strong y confinement significantly reduces simulation time.

To further our understanding, we have complemented the atomistic calculations with an effective mass (EM) based analytic model with Rashba and Dresselhaus-like SOI terms [supplementary section S1], as used in earlier works^{24,29-31}. We have also developed an analytic model to capture the effects of the inhomogeneous magnetic field [supplementary section S2]. The contributions of the SOI and ΔB on $f_{v-} - f_{v+}$ obtained from these models are shown in equations Eq. S3 and Eq. S4 respectively.

$$\Delta(f_{v-} - f_{v+})^{\text{SOI}} \approx \frac{4\pi |e| \langle z \rangle}{h^2} B_{\text{ext}} \left\{ (\beta_- - \beta_+) \sin 2\phi - (\alpha_- - \alpha_+) \right\} \quad (1)$$

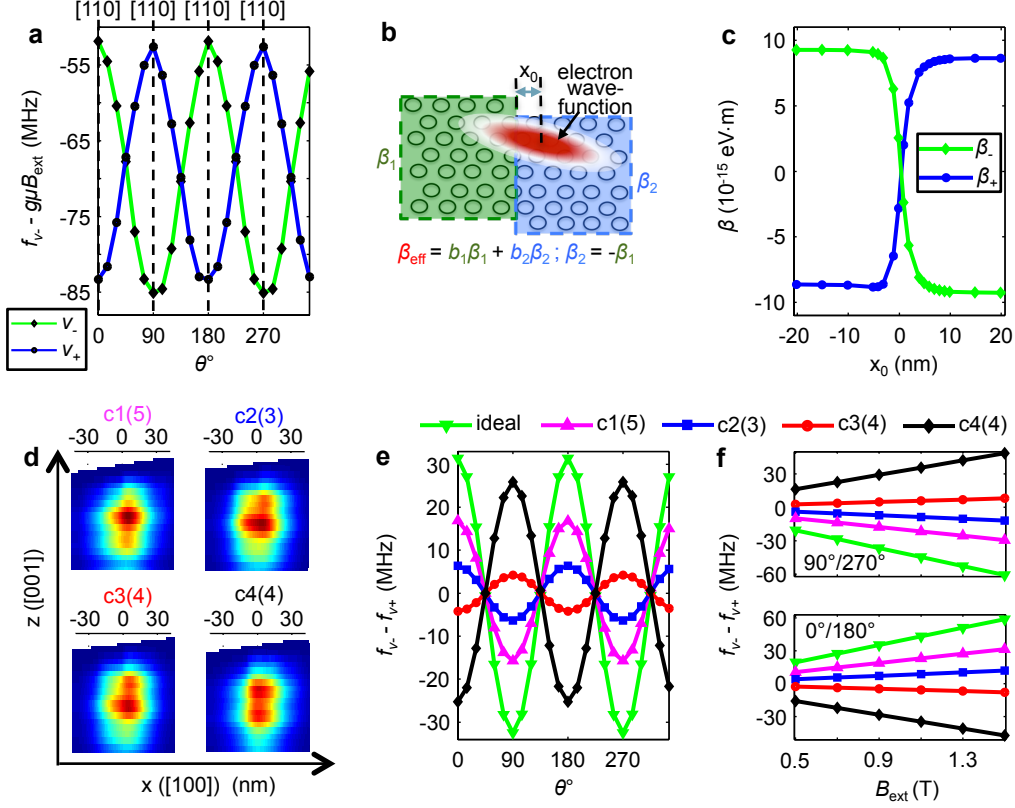


FIG. 3. **Effect of the intrinsic SOI on $f_{v\pm}$ in a Si QD.** **a**, Calculated $f_{v\pm}$ as a function of θ , in a QD with ideal (flat) interface, for $B_{\text{ext}} = 0.8$ T, without any micro-magnet. The anisotropies in these curves are in the MHz range and will appear flat on a GHz scale, like the SOI line (labeled B_{ext} (TB)) of Fig. 1d. **b**, Schematic of a QD wavefunction near a monoatomic step at the interface. The distance between the dot center and the step edge is denoted by x_0 . **c**, Computed Dresselhaus parameters β_{\pm} as a function of x_0 . β_{\pm} changes sign between the two sides of the step. **d**, QD wave-functions subjected to multiple interface steps. Four different cases are shown (c1(5), c2(3), c3(4), c4(4)) that are used in Figs. 3e, 3f and also in Figs. 4c and 4d. The number in parentheses is the total number of steps within the QD. c3 is the step configuration used in Figs. 1 and 2. **e**, Calculated $f_{v-} - f_{v+}$ as a function of θ , for different interface conditions, for $B_{\text{ext}} = 0.8$ T. Interface steps affect both the magnitude and sign of $f_{v-} - f_{v+}$. **f**, $f_{v-} - f_{v+}$ with respect to B_{ext} along $[110](\theta = 0^\circ)/[\bar{1}\bar{1}0](\theta = 180^\circ)$ (bottom panel) and $[1\bar{1}0](\theta = 90^\circ)/[110](\theta = 270^\circ)$ (top panel). $f_{v-} - f_{v+}$ for c3 (red lines with circular marker), in both Figs. 3e and 3f, corresponds to the SOI lines (blue dashed lines with diamond marker) of Figs. 1c and 2a. The parabolic confinement and E_z used here are the same as that of Figs. 1 and 2, except for Fig. 3c, where a smaller dot (with a parabolic confinement in both x and y corresponding to orbital energy splitting of 9.4 meV) is used to accommodate for large variation in dot location.

$$\Delta(f_{v-} - f_{v+})^{\Delta B} \approx \frac{g\mu}{h} \left\{ \cos \phi \left((\langle x_- \rangle - \langle x_+ \rangle) \frac{dB_x^\phi}{dx} + (\langle y_- \rangle - \langle y_+ \rangle) \frac{dB_x^\phi}{dy} \right) + \sin \phi \left((\langle x_- \rangle - \langle x_+ \rangle) \frac{dB_y^\phi}{dx} + (\langle y_- \rangle - \langle y_+ \rangle) \frac{dB_y^\phi}{dy} \right) \right\} \quad (2)$$

Here, α_{\pm} and β_{\pm} are the Rashba and Dresselhaus-like coefficients respectively, $\langle z \rangle$ is the spread of the electron wavefunction along z , $\langle x_{\pm} \rangle$ and $\langle y_{\pm} \rangle$ are the intra-valley dipole matrix elements, ϕ is the angle of the external magnetic field with respect to the $[100]$ crystal orientation and $\frac{dB_i^\phi}{dj}$ are the magnetic field gradients along

different directions ($i, j = x, y, z$) for a specific angle ϕ . It is clear from these expressions that to match $f_{v-} - f_{v+}$ the difference in SOI and dipole moment parameters between the valley states are relevant (but not their absolute values). The parameters used to match the experiment are $\alpha_- - \alpha_+ = -2.5370 \times 10^{-15}$ eV.m, $\beta_- - \beta_+ = 9.4564 \times 10^{-19}$ eV.m, $\langle x_- \rangle - \langle x_+ \rangle = -0.169$ nm, $\langle y_- \rangle - \langle y_+ \rangle = 0$ nm and $\langle z \rangle = 2.792$ nm. These fitting parameters and the separable effects of SOI and ΔB in the EM calculations enable us to obtain an even better match with the experimental data compared to TB in Figs. 1c and 2a (cyan solid lines). In contrast, in the atomistic TB calculations, we include no new fitting parameters and the effects of SOI and ΔB are intertwined by the effects of interface steps, electric field, and dot size.

As shown in Figs. 1 and 2, three physical attributes play a key role in explaining the experimental data, 1) SOI, 2) $\mathbf{B}_{\text{micro}}$, and 3) $\Delta\mathbf{B}$. Each of these contribute to $f_{v\pm}$, and only their sum can accurately reproduce the experimental data for a specific interface condition and vertical electric field, the two knobs mentioned in earlier paragraph. In Figs. 3 and 4, we show separately the effects of 1) and 3) respectively. We show how the contributions of SOI and $\Delta\mathbf{B}$ are modulated by the nature of the confining interface (knob 2). The influence of E_z (knob 1) on the effects of SOI and $\Delta\mathbf{B}$ are shown in the supplementary Figs. S3 and S4 respectively. We also show how $\mathbf{B}_{\text{micro}}$ modifies the total homogeneous B-field in the supplementary Fig. S7.

Fig. 3a shows the angular dependence of $f_{v\pm}$ for a Si QD with a smooth interface calculated from TB. Both f_{v-} and f_{v+} show a 180° periodicity but they are 90° out of phase. From analytic effective mass study [supplementary equation S11], we understand that the anisotropic contribution from the Dresselhaus-like interaction, caused by interface inversion asymmetry³¹, results in this angular dependence in $f_{v\pm}$. Moreover, the different signs of the Dresselhaus coefficients β_{\pm} for the valley states, give rise to a 90° phase shift between f_{v-} and f_{v+} . It is important to notice that the change in $f_{v\pm}$ is in MHz range. So, in GHz scale, like the blue curve (diamond markers) in Fig. 1 d, this change is not visible. However, if we compare f_{v-} and f_{v+} for this ideal interface case, we see $f_{v-} > f_{v+}$ at $\theta = 0^\circ$ and $f_{v-} < f_{v+}$ at $\theta = 90^\circ$, which does not explain the experimentally measured anisotropy. We now discuss the remaining physical parameters needed to obtain a complete understanding of the experiment.

It is well-known that the interface between Si/SiGe or Si/SiO₂ has atomic-scale disorder, with monolayer atomic steps being a common form of disorder³². To understand how such non-ideal interfaces can affect SOI, we first introduce a monolayer atomic step as shown in Fig. 3b and vary the dot position laterally relative to the step, as defined by the variable x_0 . By fitting the EM solutions to the TB results [supplementary equation S15], we have extracted the Dresselhaus-like coefficient β_{\pm} and plotted it in Fig. 3c as a function of x_0 . It is seen that β_{\pm} changes sign as the dot moves from the left to the right of the step edge. Both the sign and magnitude of β_{\pm} depends on the distribution of the wavefunction between the neighboring regions with one atomic layer shift between them, as shown in fig. 3b. A monoatomic shift of the vertical position of the interface results in a 90° rotation of its atomic arrangements about the [001] axis, which results in a sign inversion of the Dresselhaus coefficient of that region³¹. A dot wavefunction spread over a monoatomic step therefore samples out a weighted average of two β s with opposite signs^{29,30}.

Next, we investigate the anisotropy of $f_{v-} - f_{v+}$ (Fig. 3e) with various step configurations shown in Fig. 3d. $f_{v-} - f_{v+}$ in Fig. 3e exhibits a 180° periodicity, with extrema at the [110], $[\bar{1}\bar{1}0]$, $[\bar{1}10]$, $[1\bar{1}0]$ crystal orientations.

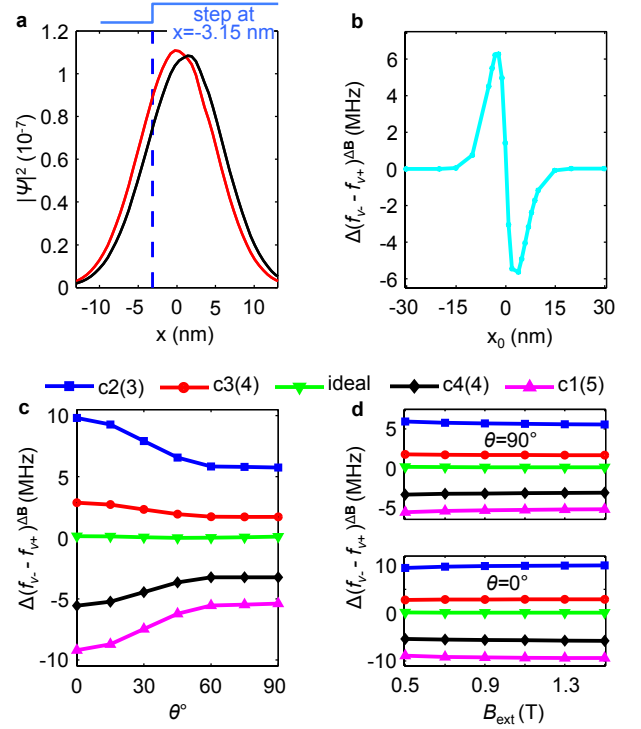


FIG. 4. Effect of inhomogeneous magnetic field on $f_{v-} - f_{v+}$. **a**, 1D cut of the wavefunctions of the two valley states close to a step edge, highlighting their spatial differences. A large vertical E-field, $E_z = 30 \text{ MVm}^{-1}$ is used here to show a magnified effect. **b**, The change in $f_{v-} - f_{v+}$ due to the inhomogeneous B-field ($\Delta\mathbf{B}$) alone as a function of the distance x_0 between the dot center and a step edge, as defined in Fig. 3b. **c**, Angular dependence of $\Delta(f_{v-} - f_{v+})^{\Delta\mathbf{B}}$ for the various step configurations of Fig. 3d (same color code) computed from atomistic TB. **d**, $\Delta(f_{v-} - f_{v+})^{\Delta\mathbf{B}}$ as a function of B_{ext} . $\Delta(f_{v-} - f_{v+})^{\Delta\mathbf{B}}$ shows negligible dependence on B_{ext} . $\Delta(f_{v-} - f_{v+})^{\Delta\mathbf{B}}$ for c3 (red lines with circular marker), in Figs. 4c and 4d, corresponds to the contribution of $\Delta\mathbf{B}$ (the difference between the black solid curve/lines with circular markers and green dashed curve/lines with square markers) of Figs. 1c and 2a. The fields used in the simulations of c and d are the same as that of Figs. 1 and 2, whereas the fields used for b are the same as that of Fig. 3c.

Both the sign and magnitude of $f_{v-} - f_{v+}$ depends on the interface condition. Since β_{\pm} decreases when a QD wavefunction is spread over a step edge, the smooth interface case (green curve) has the highest amplitude. Fig. 3f shows that the slope of $f_{v-} - f_{v+}$ with B_{ext} changes sign for a 90° rotation of \mathbf{B}_{ext} and is strongly dependent on the step configuration. The step configuration labeled c3 in Fig. 3d is used to match the experiment in Figs. 1 and 2. So the curves for c3 in both Figs. 3e and 3f correspond to the SOI results of Figs. 1c and 2a. It is key to note here that, as E_z also influences $|f_{v-} - f_{v+}|$ and $\left| \frac{d(f_{v-} - f_{v+})}{dB_{\text{ext}}} \right|$, shown in supplementary Fig. S3, a different combination of interface steps and E_z can also produce these same SOI results of Figs. 1c and 2a, but might not result in

the necessary contribution from micro-magnet to match the experiment. Now the dependence of $f_{v_-} - f_{v_+}$ on the interface condition will cause device-to-device variability, while the dependence on the direction and magnitude of \mathbf{B}_{ext} can provide control over the difference in spin splittings. These results thus give us answers to the questions 1 and 3 asked in paragraph 3.

Fig. 4 illustrates how the inhomogeneous magnetic field alone changes $f_{v_-} - f_{v_+}$ (denoted as $\Delta(f_{v_-} - f_{v_+})^{\Delta\mathbf{B}}$). Since $\Delta\mathbf{B}^{\theta}$ vectorially adds to \mathbf{B}_{ext} , an anisotropic $\Delta(f_{v_-} - f_{v_+})^{\Delta\mathbf{B}}$ is seen in Fig. 4c with and without the various step configurations portrayed in Fig. 3d. We also see that $\Delta(f_{v_-} - f_{v_+})^{\Delta\mathbf{B}}$ in Fig. 4c is negligible for a flat interface, but is significant when interface steps are present. This can be understood from Figs. 4a and 4b, and/or equation Eq. S4. Interface steps generate strong valley-orbit hybridization³³⁻³⁵ causing the valley states to have non-identical wavefunctions, and hence different dipole moments, $(\langle x_- \rangle - \langle x_+ \rangle) \neq 0$ and/or $(\langle y_- \rangle - \langle y_+ \rangle) \neq 0$, as opposed to a flat interface case, which has $\langle x_{\pm} \rangle = \langle y_{\pm} \rangle = 0$. Thus the spatially varying magnetic field has a different effect on the two wavefunctions, thereby contributing to the difference in ESR frequencies between the valley states. Fig. 4b shows $\Delta(f_{v_-} - f_{v_+})^{\Delta\mathbf{B}}$ as a function of the dot location relative to a step edge, x_0 (as in Fig. 3b) and illustrates that $\Delta\mathbf{B}$ has the largest contribution to $f_{v_-} - f_{v_+}$ when the step is in the vicinity of the dot. Also, $\Delta(f_{v_-} - f_{v_+})^{\Delta\mathbf{B}}$ is almost independent of B_{ext} , as shown in Fig. 4d. The curves labeled c3 in both Figs. 4c and 4d correspond to the contribution of $\Delta\mathbf{B}$ in Figs. 1c and 2a. Now E_z also influences $|\Delta(f_{v_-} - f_{v_+})^{\Delta\mathbf{B}}|$, as shown in supplementary Fig. S4. Thus a different combination of interface steps and E_z can also produce these same $\Delta\mathbf{B}$ results of Figs. 1c and 2a, but might not result in the necessary SOI contribution to match the experiment.

A comparison between Figs. 3f and 4d (also between equations Eq. S3 and Eq. S4) reveals that any dependence of $f_{v_-} - f_{v_+}$ on B_{ext} can only come from the SOI. This indicates that the experimental B-field dependency in Fig. 2a can not be explained without the SOI. So the effect of the SOI cannot be ignored even in the presence of a micro-magnet and this answers question 2 raised in the third paragraph. However, engineering the micro-magnetic field will allow us to engineer the anisotropy of $f_{v_-} - f_{v_+}$ (question 3, paragraph 3). Also, the influence of interface steps will cause additional device-to-device variability (question 1, paragraph 3).

The coupled spin and valley behavior observed in this work may in principle enable us to simultaneously use the quantum information stored in both spin and valley degrees of freedom of a single electron. For example, a valley controlled not gate⁹ can be designed in which the spin basis can be the target qubit, while the valley information can work as a control qubit. If we choose such a direction of the external magnetic field, where the valley states have different spin splittings, an applied microwave pulse in resonance with the spin splitting of

v_- , will rotate the spin only if the electron is in v_- . So we get a NOT operation of the spin quantum information controlled by the valley quantum information. Spin transitions conditional to valley degrees of freedom are also shown in ref. [14] and an inter-valley spin transition, which can entangle spin and valley degrees of freedom, is observed in ref. [26].

To conclude, we experimentally observe anisotropic behavior in the electron spin resonance frequencies for different valley states in a Si QD with integrated micro-magnets. We analyze this behavior theoretically and find that intrinsic SOI introduces 180° periodicity in the difference in the ESR frequencies between the valley states, but the inhomogeneous B-field of the micro-magnet also modifies this anisotropy. Interfacial non-idealities like steps control both the sign and magnitude of this difference through both SOI and inhomogeneous B-field. We also measure the external magnetic field dependence of the resonance frequencies. We show that the measured magnetic field dependence of the difference in resonance frequencies originates only from the SOI. We conclude that even though the SOI in bulk silicon has been typically ignored as being small, it still plays a major role in determining the valley dependent spin properties in interfacially confined Si QDs. These understandings help us answer the questions raised in paragraph 3, which are crucial for proper operation of various qubit schemes based on silicon quantum dots.

METHODS

For the theoretical calculations, we used a large scale atomistic tight binding approach with spin resolved $\text{sp}^3\text{d}^5\text{s}^*$ atomic orbitals with nearest neighbor interactions^{36,37}. Typical simulation domains comprise of 1.5-2 million atoms to capture realistic sized dots. Spin-orbit interactions are directly included in the Hamiltonian as a matrix element between p-orbitals following the prescription of Chadi³⁸. The advantage of this approach is that no additional fitting parameters are needed to capture various types of SOI such as Rashba and Dresselhaus SOI in contrast to k.p theory. We introduce monoatomic steps as a source of non-ideality consistent with other works^{32,35,39}. The Si interface was modeled with Hydrogen passivation⁴⁰, without using SiGe. This interface model is sufficient to capture the SOI effects of a Si/SiGe interface discussed in refs. [29-31]. We have used the methodology of ref. [28] to model the micro-magnetic fields [supplementary section S4]. Full magnetization of the micro-magnet is assumed. This causes the value of the magnetization of the micro-magnet to be saturated and makes it independent of B_{ext} . However, a change in the direction of B_{ext} changes the magnetization. We include the effect of inhomogeneous magnetic field perturbatively, with the perturbation matrix elements, $\langle \psi_m | \frac{1}{2}g\mu\Delta\mathbf{B}^{\phi} | \psi_n \rangle = \frac{1}{2}g\mu \sum_{i,j} \langle \psi_m | \frac{dB_i^{\phi}}{dj} j | \psi_n \rangle$.

Here, ψ_n and ψ_m are atomistic wave-functions calculated with homogeneous magnetic field. For further details

about the numerical techniques, see NEMO3D references [36, 37]. Method details about the experiment can be found in ref. [14].

-
- [1] Datta, S. & Das, B. Electronic analog of the electro-optic modulator. *Appl. Phys. Lett.* **56**, 665(R) (1990).
 - [2] Wolf, S. *et al.* Spintronics: A spin based electronics vision for the future. *Science* **294**, 1488-1495 (2001).
 - [3] I. Žutić, Fabian, J. & Das Sarma, S. Spintronics: Fundamentals and applications. *Rev. Mod. Phys.* **76**, 323 (2004).
 - [4] Loss, D. & Vincenzo, D. P. Quantum computation with quantum dots. *Phys. Rev. A* **57**, 120 (1998).
 - [5] Petta, J. *et al.* Coherent manipulation of coupled electron spins in semiconductor quantum dots. *Science* **309**, 2180-2184 (2005).
 - [6] Koppens, F. *et al.* Driven coherent oscillations of a single electron spin in a quantum dot. *Nature* **442**, 766-771 (2006).
 - [7] Hanson, R., Kouwenhoven, L. P., Petta, J. R., Tarucha, S., Vandersypen & L. M. K. Spins in few electron quantum dots. *Rev. Mod. Phys.* **79**, 1217 (2007).
 - [8] Xiao, D., Liu, G.-B., Feng, W., Xu, X. & Yao, W. Coupled spin and valley physics in monolayers of MoS₂ and other group VI dichalcogenides. *Phys. Rev. Lett.* **108**, 196802 (2012).
 - [9] Gong, Z. *et al.* Magnetoelectric effects and valley-controlled spin quantum gates in transition metal dichalcogenide bilayers. *Nature Communications* **4**, 2053 (2013).
 - [10] Xu, X., Yao, W., Xiao, D. & Heinz, T. Spins and pseudospins in layered transition metal dichalcogenides. *Nature Physics* **10**, 343350 (2014).
 - [11] Renard, V. T. *et al.* Valley polarization assisted spin polarization in two dimensions. *Nature Communications* **6**, 7230 (2015).
 - [12] Yang, C. *et al.* Spin-valley lifetimes in a silicon quantum dot with tunable valley splitting. *Nature Communications* **4**, 2069 (2013).
 - [13] Hao, X., Ruskov, R., Xiao, M., Tahan, C. & Jiang, H. Electron spin resonance and spin-valley physics in a silicon double quantum dot. *Nature Communications* **5**, 3860 (2014).
 - [14] Kawakami, E. *et al.* Electrical control of a long-lived spin qubit in a Si/SiGe quantum dot. *Nature Nanotechnology* **9**, 666670 (2014).
 - [15] Veldhorst, M. *et al.* An addressable quantum dot qubit with fault tolerant control fidelity. *Nature Nanotechnology* **9**, 981985 (2014).
 - [16] Maune, B. M. *et al.* Coherent singlet-triplet oscillations in a silicon-based double quantum dot. *Nature* **481**, 344347 (2011).
 - [17] Wu, X. *et al.* Two-axis control of a singlet-triplet qubit with integrated micromagnet. *Proc. Natl. Acad. Sci. USA* **111**, 11938 (2014).
 - [18] Eng, K. *et al.* Isotopically enhanced triple quantum dot qubit. *Science Advances* **1**, no. 4, e1500214 (2015).
 - [19] Kim, D. *et al.* Quantum control and process tomography of a semiconductor quantum dot hybrid qubit. *Nature* **511**, 70-74 (2014).
 - [20] Kim, D. *et al.* High fidelity resonant gating of a silicon-based quantum dot hybrid qubit. *npj Quantum Informa-*
 - tion* **1** 15004 (2015).
 - [21] Culcer, D., Sariaeva, A. L., Koiller, B., Hu, X. & Das Sarma, S. Valley-based noise resistant quantum computation using Si quantum dots. *Phys. Rev. Lett.* **108**, 126804 (2012).
 - [22] Rohling, N. & Burkard, G. Universal quantum computing with spin and valley states. *New J. Phys.* **14**, 083008 (2012).
 - [23] Rohling, N., Russ, M. & Burkard, G. Hybrid spin and valley quantum computing with singlet-triplet qubits. *Phys. Rev. Lett.* **113**, 176801 (2014).
 - [24] Veldhorst, M. *et al.* Spin-orbit coupling and operation of multivalley spin qubits. *Phys. Rev. B* **92**, 201401(R) (2015).
 - [25] Scarlino, P. *et al.* Second-harmonic coherent driving of a spin qubit in SiGe/Si quantum dot. *Phys. Rev. Lett.* **115**, 106802 (2015).
 - [26] Scarlino, P. *et al.*, Dressed photon-orbital states in a quantum dot: Inter-valley spin resonance, *arXiv*: 1608.06538 (2016).
 - [27] Tokura, Y., van der Wiel, W. G., Obata, T. & Tarucha, S. Coherent single electron spin control in a slanting Zeeman field. *Phys. Rev. Lett.* **96**, 047202 (2006).
 - [28] Goldman, J. R., Ladd, T. D., Yamaguchi, F. & Yamamoto, Y. Magnet designs for a crystal lattice quantum computer. *Appl. Phys. A* **71**, 11 (2000).
 - [29] Golub, L. E., & Ivchenko, E. L. Spin splitting in symmetrical SiGe quantum wells. *Phys. Rev. B* **69**, 115333 (2004).
 - [30] Nestoklon, M. O., Golub, L. E. & Ivchenko, E. L. Spin and valley-orbit splittings in SiGe/Si heterostructures. *Phys. Rev. B* **73**, 235334 (2006).
 - [31] Nestoklon, M. O., Ivchenko, E. L., Jancu, J. -M. & Voisin, P. Electric field effect on electron spin splitting in SiGe/Si quantum wells. *Phys. Rev. B* **77**, 155328 (2008).
 - [32] Zandvliet, H. J. W. & Elswijk, H. B. Morphology of monatomic step edges on vicinal Si(001). *Phys. Rev. B* **48**, 14269 (1993).
 - [33] Gamble, J. K., Eriksson, M. A., Coppersmith, S. N. & Friesen, M. Disorder-induced valley-orbit hybrid states in Si quantum dots. *Phys. Rev. B* **88**, 035310 (2013).
 - [34] Friesen, M., & Coppersmith, S. N. Theory of valley-orbit coupling in a Si/SiGe quantum dot. *Phys. Rev. B* **81**, 115324 (2010).
 - [35] Friesen, M., Eriksson, M. A. & Coppersmith, S. N. Magnetic field dependence of valley splitting in realistic Si/SiGe quantum wells, *Appl. Phys. Lett.* **89**, 202106 (2006).
 - [36] Klimeck, G. *et al.* Atomistic simulation of realistically sized nanodevices using NEMO 3D: Part I—models and benchmarks. *IEEE Trans. Electron Dev.* **54**, 2079-2089 (2007).
 - [37] Klimeck, G., Oyafuso, F., Boykin, T., Bowen, R., & Allen, P. Development of a nanoelectronic 3D (NEMO-3D) simulator for multimillion atom simulations and its application to alloyed quantum dots, *Computer Modeling in Engineering and Sciences (CMES)* **3**, No. 5, 601-642

(2002).

- [38] Chadi, D. J. Spin-orbit splitting in crystalline and compositionally disordered semiconductors. *Phys. Rev. B* **16**, 790 (1977).
- [39] Kharche, N., Prada, M., Boykin, T. B. & Klimeck, G. Valley splitting in strained silicon quantum wells modeled with 2 miscuts, step disorder, and alloy disorder. *Appl. Phys. Lett.* **90**, 092109 (2007).
- [40] Lee, S., Oyafuso, F., Allmen, P. V. & Klimeck, G. Boundary conditions for the electronic structure of finite-extent embedded semiconductor nanostructures. *Phys. Rev. B* **69**, 045316 (2004).

ACKNOWLEDGMENTS

This work was supported in part by ARO (W911NF-12-0607); development and maintenance of the growth facilities used for fabricating samples is supported by DOE (DE-FG02-03ER46028). This research utilized NSF-supported shared facilities at the University of Wisconsin-Madison. Computational resources on nanoHUB.org, funded by the NSF grant EEC-0228390, were used. M.P.N. acknowledges support from ERC Synergy Grant. R.F. and R.R. acknowledge discussions with R. Ruskov, C. Tahan, and A. Dzurak.

AUTHOR CONTRIBUTIONS STATEMENT

R.F. performed the g-factor calculations, explained the underlying physics and developed the theory with guidance from R.R. R.F., R.R., E.K., P.S., and M.P.N. analyzed the simulation results and compared with experimental data in consultation with L.M.K.V., M.F., S.N.C. and M.A.E.. E.K. and P.S. performed the experiment and analyzed the measured data. D.R.W. fabricated the sample. D.E.S. and M.G.L. grew the heterostructure. R.F. and R.R. wrote the manuscript with feedback from all the authors. R.R. and L.M.K.V. initiated the project, and supervised the work with S.N.C, M.F. and M.A.E.

ADDITIONAL INFORMATION

The authors declare that they have no competing financial interests.

SUPPLEMENTARY MATERIALS FOR ‘VALLEY DEPENDENT ANISOTROPIC SPIN SPLITTING IN SILICON QUANTUM DOTS’

S1. Analytic effective mass model to explain the effect of spin-orbit interaction (SOI) on the valley dependent g-factor anisotropy in a silicon quantum dot

To explain our atomistic tight-binding (TB) results of the valley dependent g-factor and its anisotropy in a silicon quantum dot (QD), we have also performed analytic effective mass calculations as shown here. The electron Hamiltonian can be written as,

$$H = \frac{\hbar^2}{2m} \mathbf{k}^2 + V(\mathbf{r}) + H_Z + H_{SO} \quad (\text{Eq. S3})$$

Here, m is the electron effective mass, which assumes a value of $0.19m_0$ and $0.91m_0$ for the transverse (x or [100], y or [010]) and longitudinal (z or [001]) components in Si respectively (m_0 being the free electron mass). $V(\mathbf{r})$ is the potential defining the quantum dot, and has been discussed in the main text. $H_Z = \frac{1}{2}g\mu\boldsymbol{\sigma} \cdot \mathbf{B}$ is the Zeeman term, with g the electron g -factor, μ the Bohr magneton, and \mathbf{B} the applied magnetic field at the dot location. $H_{SO} = \beta(\sigma_x k_x - \sigma_y k_y) + \alpha(\sigma_x k_y - \sigma_y k_x)$ is the SOI term, where β (α) is the strength of Dresselhaus (Rashba) interaction, σ_x, σ_y are the Pauli spin matrices, and k_x (k_y) is electron canonical momentum along x (y) direction. $\mathbf{k} = -i\nabla - e\frac{\mathbf{A}}{\hbar}$, where \mathbf{A} is the vector potential and $\mathbf{B} = \nabla \times \mathbf{A}$. Now, we treat $H_P = \frac{1}{2}g\mu\boldsymbol{\sigma} \cdot \mathbf{B} + \beta(\sigma_x k_x - \sigma_y k_y) + \alpha(\sigma_x k_y - \sigma_y k_x)$ as a perturbation to $H_0 = \frac{\hbar^2}{2m} \mathbf{k}^2 + V(\mathbf{r})$. The unperturbed Hamiltonian H_0 yields the spin degenerate eigenstates of a Si QD. Typically, in these devices, orbital splitting (E_{OS}) is much larger than valley (E_{VS}) and spin (E_{ZS}) splittings. So, we only consider the four lowest energy states $|\psi_{v-}^\downarrow\rangle, |\psi_{v-}^\uparrow\rangle, |\psi_{v+}^\downarrow\rangle, |\psi_{v+}^\uparrow\rangle$ as the basis for the perturbation calculation. We can write the perturbation Hamiltonian as,

$$H_P = \sigma_x \left(\frac{1}{2}g\mu B_x + \beta k_x + \alpha k_y \right) + \sigma_y \left(\frac{1}{2}g\mu B_y - \beta k_y - \alpha k_x \right) + \sigma_z \left(\frac{1}{2}g\mu B_z \right) \quad (\text{Eq. S4})$$

After diagonalizing S2, we obtain the spin splittings for different valley states,

$$E_{ZS(\pm)} = 2 \left\{ \left(\frac{1}{2}g\mu B_z \right)^2 + \left(\frac{1}{2}g\mu B_x + \beta_\pm \langle k_x^\pm \rangle + \alpha_\pm \langle k_y^\pm \rangle \right)^2 + \left(\frac{1}{2}g\mu B_y - \beta_\pm \langle k_y^\pm \rangle - \alpha_\pm \langle k_x^\pm \rangle \right)^2 \right\}^{\frac{1}{2}} \quad (\text{Eq. S5})$$

Here, we replaced β, α with β_\pm, α_\pm to denote the two v_+ and v_- valley states^{1,2}. Now, the expectation values of the momentum operator in a magnetic field \mathbf{B} are,

$$\langle k_x^\pm \rangle = \langle \psi_{v\pm} | -i \frac{\partial}{\partial x} - e \frac{A_x}{\hbar} | \psi_{v\pm} \rangle \approx |e| \frac{\langle A_x^\pm \rangle}{\hbar} \quad (\text{Eq. S6})$$

$$\langle k_y^\pm \rangle = \langle \psi_{v\pm} | -i \frac{\partial}{\partial y} - e \frac{A_y}{\hbar} | \psi_{v\pm} \rangle \approx |e| \frac{\langle A_y^\pm \rangle}{\hbar} \quad (\text{Eq. S7})$$

Since $\langle \psi_{v\pm} | -i \frac{\partial}{\partial x} | \psi_{v\pm} \rangle \approx \langle \psi_{v\pm} | -i \frac{\partial}{\partial y} | \psi_{v\pm} \rangle \approx 0$. For a magnetic field in the x-y plane, we assume, $A_z = 0$, $A_x = zB_y$ and $A_y = -zB_x$, where B_x and B_y are the x and y components of the magnetic field respectively. Then,

$$\langle k_x^\pm \rangle \approx |e| \frac{\langle z \rangle}{\hbar} B_y \quad (\text{Eq. S8})$$

$$\langle k_y^\pm \rangle \approx -|e| \frac{\langle z \rangle}{\hbar} B_x \quad (\text{Eq. S9})$$

Here, $\langle z \rangle$ is the dipole moment along [001] crystal direction. We assumed $\langle z_- \rangle = \langle z_+ \rangle = \langle z \rangle$. As the electrons in the v_- and v_+ valley states have only z valley component, we can replace g here with g_\perp , the g -factor perpendicular to the valley axis⁴. So, for an in-plane magnetic field,

$$E_{\text{ZS}(\pm)} = 2 \left\{ \left(\frac{1}{2} g_{\perp} \mu B_x + \beta_{\pm} |e| \frac{\langle z \rangle}{\hbar} B_y - \alpha_{\pm} |e| \frac{\langle z \rangle}{\hbar} B_x \right)^2 + \left(\frac{1}{2} g_{\perp} \mu B_y + \beta_{\pm} |e| \frac{\langle z \rangle}{\hbar} B_x - \alpha_{\pm} |e| \frac{\langle z \rangle}{\hbar} B_y \right)^2 \right\}^{\frac{1}{2}} \quad (\text{Eq. S10})$$

In the presence of only external magnetic field, \mathbf{B}_{ext} , $B_x = B_{\text{ext}} \cos \phi$ and $B_y = B_{\text{ext}} \sin \phi$, with ϕ being the B-field angle relative to the [100] crystal orientation for a counter clockwise rotation of B_{ext} . However, to be consistent with the angle θ defined in the experiment (i.e. an angle relative to the [110] crystal orientation with clockwise rotation of \mathbf{B}_{ext}), we use the relation $\theta = 45^\circ - \phi$. Now, using the definition of B_x and B_y from above, we can obtain the angular dependence of the spin splitting for different valley states,

$$E_{\text{ZS}(\pm)} = g_{\perp} \mu B_{\text{ext}} \left\{ 1 + 4 \left(\frac{|e| \langle z \rangle}{g_{\perp} \mu \hbar} \right)^2 (\beta_{\pm}^2 + \alpha_{\pm}^2) - 4 \frac{|e| \langle z \rangle}{g_{\perp} \mu \hbar} \alpha_{\pm} + 4 \frac{|e| \langle z \rangle}{g_{\perp} \mu \hbar} \beta_{\pm} \sin 2\phi - 8 \left(\frac{|e| \langle z \rangle}{g_{\perp} \mu \hbar} \right)^2 \beta_{\pm} \alpha_{\pm} \sin 2\phi \right\}^{\frac{1}{2}} \quad (\text{Eq. S11})$$

Now, $1 \gg \left(\frac{|e| \langle z \rangle}{g_{\perp} \mu \hbar} \right) * \beta_{\pm} > \left(\frac{|e| \langle z \rangle}{g_{\perp} \mu \hbar} \right) * \alpha_{\pm}^2$. So, we can ignore the second order terms. Thus simplifying equation (S9) we get,

$$E_{\text{ZS}(\pm)} = g_{\perp} \mu B_{\text{ext}} \left\{ 1 - 4 \frac{|e| \langle z \rangle}{g_{\perp} \mu \hbar} \alpha_{\pm} + 4 \frac{|e| \langle z \rangle}{g_{\perp} \mu \hbar} \beta_{\pm} \sin 2\phi \right\}^{\frac{1}{2}} \quad (\text{Eq. S12})$$

After doing a series expansion and ignoring higher order terms, we can simplify this expression even further,

$$E_{\text{ZS}(\pm)} = g_{\perp} \mu B_{\text{ext}} \left\{ 1 - 2 \frac{|e| \langle z \rangle}{g_{\perp} \mu \hbar} \alpha_{\pm} + 2 \frac{|e| \langle z \rangle}{g_{\perp} \mu \hbar} \beta_{\pm} \sin 2\phi \right\} \quad (\text{Eq. S13})$$

So, from this equation we can see that, **without the Dresselhaus contribution, there is no angular dependence or anisotropy in the spin splitting (or g-factor) for the different valley states**. Now, for \mathbf{B}_{ext} along the [110] and $[\bar{1}\bar{1}0]$ crystal orientations, we get,

$$E_{\text{ZS}(\pm)}^{[110]} - g_{\perp} \mu B_{\text{ext}} = 2 (\beta_{\pm} - \alpha_{\pm}) |e| \frac{\langle z \rangle}{\hbar} B_{\text{ext}} \quad (\text{Eq. S14})$$

$$E_{\text{ZS}(\pm)}^{[\bar{1}\bar{1}0]} - g_{\perp} \mu B_{\text{ext}} = 2 (-\beta_{\pm} - \alpha_{\pm}) |e| \frac{\langle z \rangle}{\hbar} B_{\text{ext}} \quad (\text{Eq. S15})$$

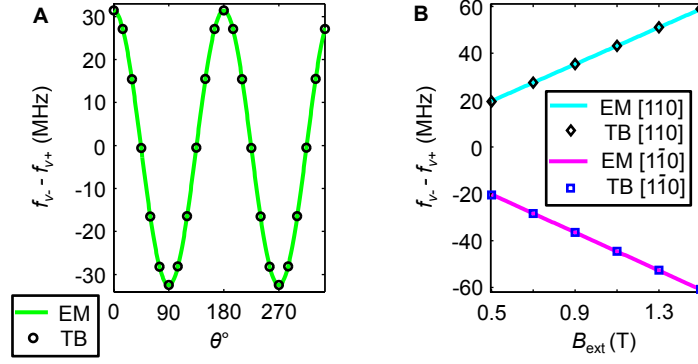
Equation (S12) matches the analytic prediction of ref. [1]. We can extract α_{\pm} and β_{\pm} from the atomistic calculations as follows,

$$\alpha_{\pm} = - \frac{(E_{\text{ZS}(\pm)}^{[110]} + E_{\text{ZS}(\pm)}^{[\bar{1}\bar{1}0]} - 2g_{\perp} \mu B_{\text{ext}})}{4 |e| \frac{\langle z \rangle}{\hbar} B_{\text{ext}}} \quad (\text{Eq. S16})$$

$$\beta_{\pm} = \frac{E_{\text{ZS}(\pm)}^{[\bar{1}\bar{1}0]} - E_{\text{ZS}(\pm)}^{[110]}}{4 |e| \frac{\langle z \rangle}{\hbar} B_{\text{ext}}} \quad (\text{Eq. S17})$$

In Fig. S1, we compared $f_{v-} - f_{v+}$ calculated from this analytic model with the atomistic tight-binding results for the ideal interface case, shown in Figs. 3e and 3f of the main text. Both the anisotropic behavior of $f_{v-} - f_{v+}$ with respect to the angle of \mathbf{B}_{ext} (Fig. S1A), and the dependence on the magnitude B_{ext} along [110] and $[\bar{1}\bar{1}0]$ crystal orientations (Fig. S1B) show perfect agreement between analytic and atomistic calculations. From the atomistic calculations of Fig. 3a and equation (S14) and (S15), we extracted $\beta_- = 10.117 \times 10^{-15} \text{eV}\cdot\text{m}$, $\beta_+ = -9.3621 \times 10^{-15} \text{eV}\cdot\text{m}$, $\alpha_- = -1.2568 \times 10^{-15} \text{eV}\cdot\text{m}$, $\alpha_+ = -1.5920 \times 10^{-15} \text{eV}\cdot\text{m}$ for $g_{\perp} = 1.9937$ and $\langle z \rangle = 2.7925 \text{ nm}$, calculated using $\langle z \rangle \approx 1.5587 l_z$, where, $l_z = \left(\frac{\hbar^2}{2m_l |e| E_z} \right)^{\frac{1}{3}}$. Here, $E_z = 6.77 \text{ MVm}^{-1}$ is the vertical electric field.

To include the homogeneous fields from the micro-magnets, in equation (S3), we use, $B_x = B_{\text{ext}} \cos \theta + B_{\text{micro}}^x(\theta)$, $B_y = B_{\text{ext}} \sin \theta + B_{\text{micro}}^y(\theta)$ and $B_z = B_{\text{micro}}^z(\theta)$. As, $B_{x/y} \gg B_z$ and $\langle x/y \rangle \gg \langle z \rangle$, we can still use equation (S6) and (S7) for $\langle k_x^{\pm} \rangle$ and $\langle k_y^{\pm} \rangle$.



Supplementary Fig. S5. Effect of spin-orbit interaction: comparison between analytic effective mass and atomistic tight-binding calculations. **A**, Comparison in angular dependence of $f_{v_-} - f_{v_+}$ for $B_{\text{ext}} = 800 \text{ mT}$. The angle of \mathbf{B}_{ext} is defined clockwise with respect to the $[110]$ crystal orientation) **B**, Magnetic field dependence of $f_{v_-} - f_{v_+}$ for \mathbf{B}_{ext} along $[110]$ and $[1\bar{1}0]$ crystal orientations. The tight-binding calculations correspond to the ideal (interface) case of Figs. 3e and 3f of the main text.

S2. Analytic model to explain the effect of gradient magnetic field on the valley dependent spin-splittings in a Si QD

To develop an analytic model to capture the effect of the inhomogeneous magnetic field on the spin-splittings for different valley states, we assume the Hamiltonian in equation (S1) as our unperturbed Hamiltonian and include the magnetic field gradient as a perturbation,

$$H_P^{\Delta\mathbf{B}} = \frac{1}{2}g\mu\boldsymbol{\sigma}\cdot\Delta\mathbf{B} = \frac{1}{2}g\mu\left\{\sum_i\sigma_i\left(\sum_j\frac{dB_i}{dj}j\right)\right\} \quad (\text{Eq. S18})$$

Here, $\frac{dB_i}{dj}$ are the magnetic field gradients along different directions, where i, j correspond to x,y,z co-ordinates. Now the lowest 4 eigen-states of the unperturbed Hamiltonian are $|v_- \downarrow\rangle$, $|v_- \uparrow\rangle$, $|v_+ \downarrow\rangle$ and $|v_+ \uparrow\rangle$. The 1st order correction due to $H_P^{\Delta\mathbf{B}}$ to $|v_- \downarrow\rangle$ is given by,

$$\Delta E_{v_- \downarrow}^{\Delta\mathbf{B}} = \langle v_- \downarrow | \frac{1}{2}g\mu\left\{\sum_i\sigma_i\left(\sum_j\frac{dB_i}{dj}j\right)\right\} | v_- \downarrow \rangle \quad (\text{Eq. S19})$$

To simplify our analytic calculation, we assume that the spin mixing due to SOI is very small and we can separate the spin part from the spatial part of the wavefunction. Using this approximation in Eq. S19, we get,

$$\Delta E_{v_- \downarrow}^{\Delta\mathbf{B}} = \frac{1}{2}g\mu\left\{\sum_i\langle\downarrow|\sigma_i|\downarrow\rangle\left(\sum_j\frac{dB_i}{dj}\langle j_- \rangle\right)\right\} \quad (\text{Eq. S20})$$

Here, $\langle j_- \rangle$ is the dipole moment along the j direction, $\langle j_- \rangle = \langle v_- | j | v_- \rangle$. Now, for spins in an in-plane magnetic field, $\langle\downarrow|\sigma_x|\downarrow\rangle = -\cos\phi$, $\langle\downarrow|\sigma_y|\downarrow\rangle = -\sin\phi$ and $\langle\downarrow|\sigma_z|\downarrow\rangle = 0$. The external magnetic field fully magnetizes the micro-magnets. So, the inhomogeneous magnetic field from the micro-magnets ($\frac{dB_i}{dj}$) depends on the direction (ϕ) of the external magnetic field. Using these relations in equation (S19) we get,

$$\Delta E_{v_- \downarrow}^{\Delta\mathbf{B}} = -\frac{1}{2}g\mu\left\{\cos\phi\left(\sum_j\langle j_- \rangle\frac{dB_x^\phi}{dj}\right) + \sin\phi\left(\sum_j\langle j_- \rangle\frac{dB_y^\phi}{dj}\right)\right\} \quad (\text{Eq. S21})$$

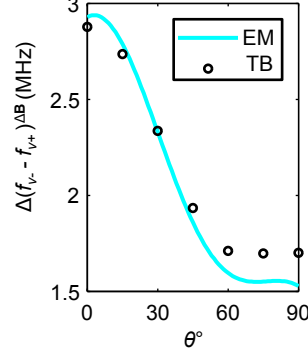
Now, for $|v_- \uparrow\rangle$, $\langle\uparrow|\sigma_x|\uparrow\rangle = \cos\phi$, $\langle\uparrow|\sigma_y|\uparrow\rangle = \sin\phi$ and $\langle\uparrow|\sigma_z|\uparrow\rangle = 0$. So,

$$\Delta E_{v_- \uparrow}^{\Delta\mathbf{B}} = \frac{1}{2}g\mu\left\{\cos\phi\left(\sum_j\langle j_- \rangle\frac{dB_x^\phi}{dj}\right) + \sin\phi\left(\sum_j\langle j_- \rangle\frac{dB_y^\phi}{dj}\right)\right\} \quad (\text{Eq. S22})$$

We can get similar expressions for $|v_+ \downarrow\rangle$ and $|v_+ \uparrow\rangle$. So, the change in spin splitting of both the valleys due to the gradient magnetic field is,

$$\Delta E_{\text{ZS}(\pm)}^{\Delta\mathbf{B}} = g\mu\left\{\cos\phi\left(\sum_j\langle j_\pm \rangle\frac{dB_x^\phi}{dj}\right) + \sin\phi\left(\sum_j\langle j_\pm \rangle\frac{dB_y^\phi}{dj}\right)\right\} \quad (\text{Eq. S23})$$

For an electron in an ideal (smooth) interface, $\langle x_\pm \rangle \approx \langle y_\pm \rangle \approx 0$. But the presence of interface steps in realistic devices makes $\langle x_\pm \rangle$ and/or $\langle y_\pm \rangle$ non zero. We can ignore the 2nd order corrections because $\frac{1}{2}g\mu\frac{dB_x^\phi}{dj}\langle j_\pm \rangle \ll E_{\text{ZS}}$. Due to interface steps, $\langle x_- \rangle \neq \langle x_+ \rangle$ and/or $\langle y_- \rangle \neq \langle y_+ \rangle$, but $\langle z_- \rangle \approx \langle z_+ \rangle$, for the electric field used in the experiment. So, in the presence of interface steps, the magnetic field gradient adds to the difference in ESR frequencies between the valley states, and from equation (S21), we get equation (3) of the main text.

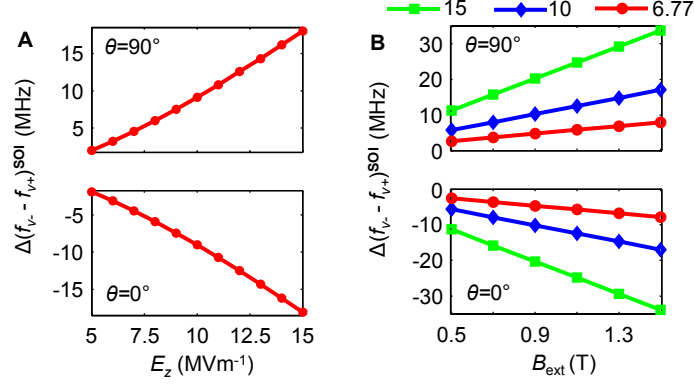


Supplementary Fig. S6. Effect of the gradient magnetic field on the anisotropy of $f_{v-} - f_{v+}$: comparison between analytic effective mass and atomistic tight-binding calculations. For the latter, the contribution of the SOI is subtracted to obtain the change in $f_{v-} - f_{v+}$ due to $\Delta\mathbf{B}$ only from Fig. 1c of the main text (difference between green dashed line and black solid line).

In Fig. S2, we compared $\Delta(f_{v-} - f_{v+})^{\Delta\mathbf{B}}$ calculated using equation (2) of the main text with atomistic tight-binding calculations. We used $\langle x_- \rangle - \langle x_+ \rangle \approx -0.17$ nm and $\langle y_- \rangle - \langle y_+ \rangle = 0$ in equation (2). The atomistic results shown in Fig. S2 is the difference between the black curve (circular marker) and the green curve (square markers) shown in Fig. 1c. The analytic calculation qualitatively captures the tight-binding results. The little mismatch between the analytic and atomistic calculation is due to ignoring the spin mixing from SOI in our analytic model.

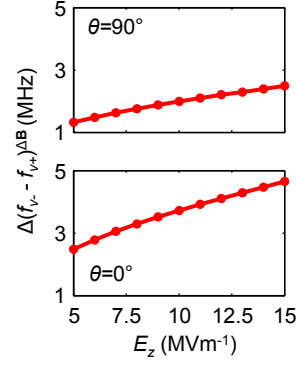
S3. Effect of the vertical electric field on the difference in ESR frequencies between valley states through both SOI and gradient magnetic field

The vertical electric field, E_z affects $f_{v_-} - f_{v_+}$, because it affects the SOI parameters² and also the dipole moment parameters. The effect of E_z on $f_{v_-} - f_{v_+}$ due to the SOI and gradient magnetic field, from atomistic tight-binding calculations, are shown in supplementary Figs. S3 and S4 respectively. Here E_z only changes the magnitude of $f_{v_-} - f_{v_+}$, but not its sign. E_z also effect the B_{ext} dependence of $f_{v_-} - f_{v_+}$ through SOI, as shown in supplementary Fig. S3B. Here also E_z only changes the magnitude of the slope, $\frac{d\Delta(f_{v_-} - f_{v_+})^{\text{SOI}}}{dB_{\text{ext}}}$ but not its sign.



Supplementary Fig. S7. Influence of the vertical electric field E_z on the change in $f_{v_-} - f_{v_+}$ due to SOI. **A**, Increase in $|\Delta(f_{v_-} - f_{v_+})^{\text{SOI}}|$ with increasing E_z for $B_{\text{ext}} = 0.8$ T. **B**, Change in $\Delta(f_{v_-} - f_{v_+})^{\text{SOI}}$ with changing B_{ext} for different E_z .

E_z changes the magnitude of the slope, $\left| \frac{d\Delta(f_{v_-} - f_{v_+})^{\text{SOI}}}{dB_{\text{ext}}} \right|$. Bottom panels in both Figs. A and B corresponds to \mathbf{B}_{ext} along $[110]$ ($\theta = 0^\circ$) and in top panels \mathbf{B}_{ext} is along $[1\bar{1}0]$ ($\theta = 90^\circ$). Interface condition and parabolic confinement for the dot used in these simulations are the same as that used to match experimental data in Figs. 1 and 2 of main text.



Supplementary Fig. S8. Influence of the vertical electric field E_z on the change in $f_{v-} - f_{v+}$ due to the gradient magnetic field $\Delta\mathbf{B}$, for \mathbf{B}_{ext} along $[110]$ $\theta = 0^\circ$ (bottom panel) and $[1\bar{1}0]$ ($\theta = 90^\circ$) (top panel). Interface condition and parabolic confinement for the dot used in these simulations are the same as that used to match experimental data in Figs. 1 and 2 of the main text. Increasing E_z increases $\left| \Delta(f_{v-} - f_{v+})^{\Delta\mathbf{B}} \right|$.

S4. Modeling the stray magnetic field induced by the micro-magnets

We calculated the local magnetic field created by the micro-magnets when the external magnetic field is applied along the y' ([110]) ($\theta = 0^\circ$) or along the x' ($[1\bar{1}0]$) axis ($\theta = 90^\circ$) of the device picture in Fig. S5, assuming that the micro-magnets are fully magnetized^{5,6}. The shape of the micro-magnets is shown in ref. [7].

Fig. S9 and Fig. S10 show the results of the numerical calculation of the total magnetic field gradient when the external magnetic field is applied along the y' axis and along the x' axis respectively, and the pink circle shows the estimated dot position.

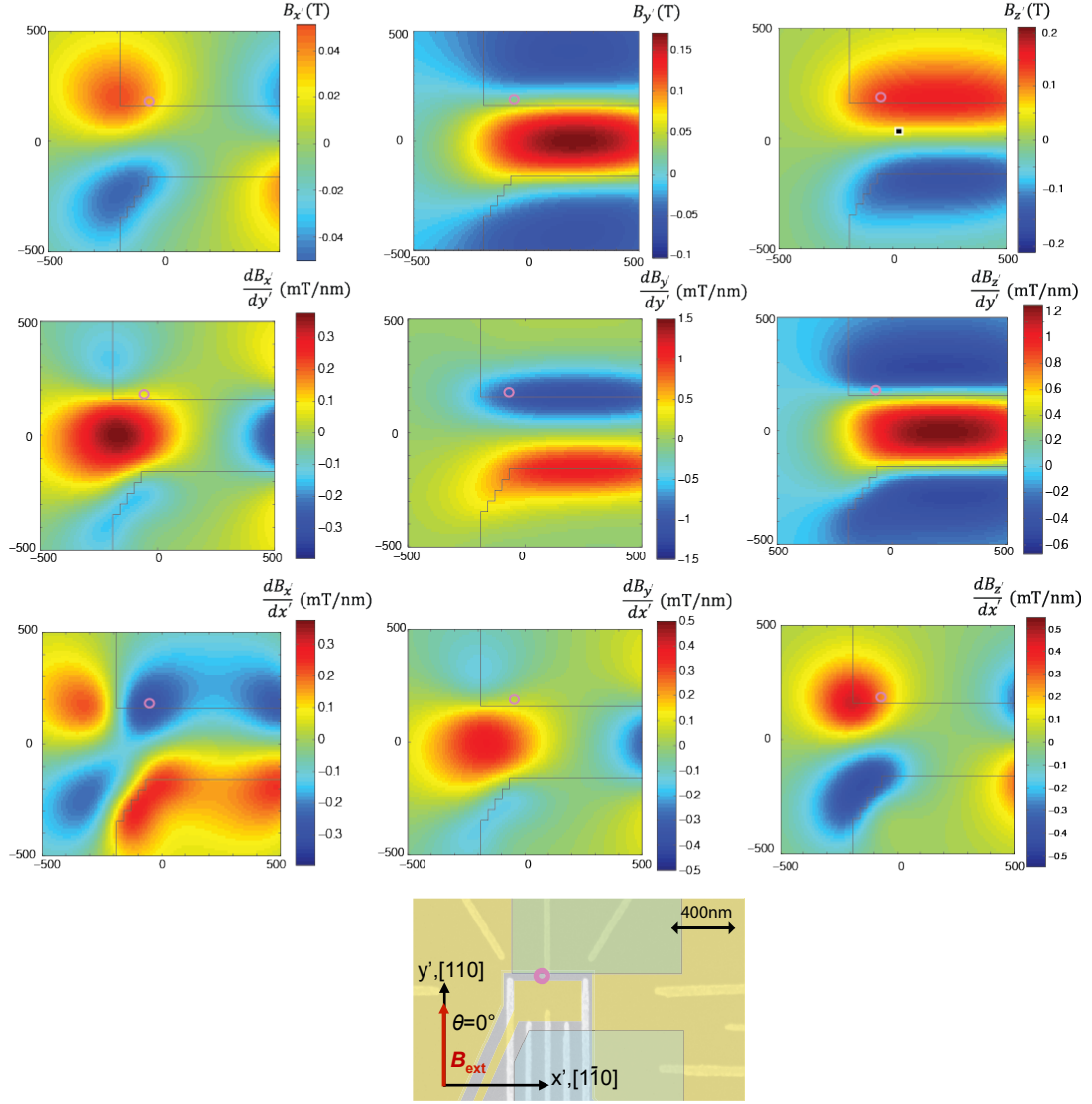
We calculated the stray magnetic field created by the micro-magnets when the external magnetic field is applied between the y' axis and the x' axis ($0^\circ < \theta < 90^\circ$) according to the following approximation,

$$B_i^\theta = \cos^2 \theta B_i^{0^\circ} + \sin^2 \theta B_i^{90^\circ}, \quad (\text{Eq. S24})$$

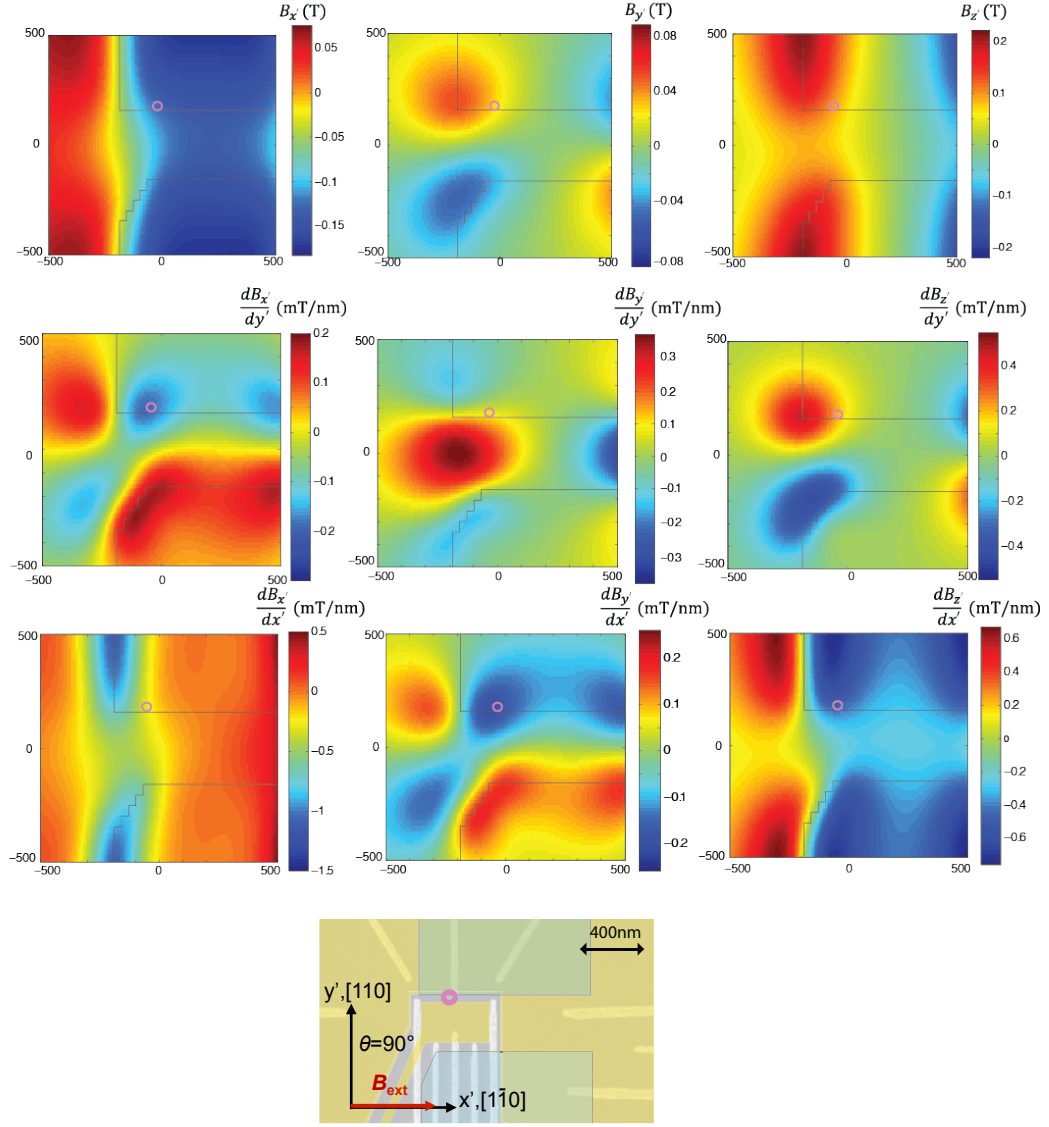
where $i = x', y', z$.

We ignore $\frac{dB_i^\theta}{dz}$, with $i = x', y', z$. For small electric field like $E_z = 6.77 \text{ MVm}^{-1}$ used to match the experiment, the electron wavefunctions of the two valley states have similar spread along z , so $\langle v_- | \frac{dB_i^\theta}{dz} z | v_- \rangle \approx \langle v_+ | \frac{dB_i^\theta}{dz} z | v_+ \rangle$. Thus the effects of $\frac{dB_i^\theta}{dz}$ on $f_{v-} - f_{v+}$ should be small. However, the effects of these $\frac{dB_i^\theta}{dz}$ on f_{v-} or f_{v+} can be larger, but as shown in the Figs. 1d and 2b of the main text, the effect of the gradient magnetic field on $f_{v\pm}$ is negligible compared to that of the homogeneous magnetic fields.

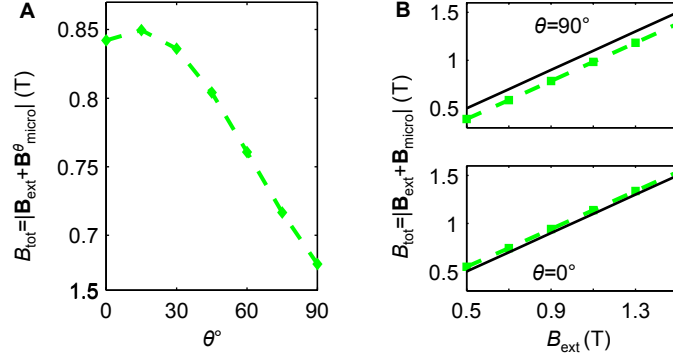
The micro-magnetic field used in our calculations are $\mathbf{B}_{\text{micro}}^{0^\circ} = (0.03, 0.03, 0.139) \text{ T}$, $\mathbf{B}_{\text{micro}}^{90^\circ} = (-0.122, 0.03, 0.089) \text{ T}$, $\frac{d\mathbf{B}^{0^\circ}}{dx'} = (-0.185, 0.056, 0.217) \text{ T/nm}$, $\frac{d\mathbf{B}^{0^\circ}}{dy'} = (-0.0653, -0.93, -0.052) \text{ T/nm}$, $\frac{d\mathbf{B}^{90^\circ}}{dx'} = (-0.272, -0.185, -0.456) \text{ T/nm}$, $\frac{d\mathbf{B}^{90^\circ}}{dy'} = (-0.184, -0.065, 0.211) \text{ T/nm}$.



Supplementary Fig. S9. Numerically computed x' , y' and z components of the magnetic field and their gradients along the x' and y' axes induced by the micro-magnets when the external magnetic field is applied along the y' axis in the plane of the Si quantum well, for fully magnetized micro-magnets. The black solid lines indicate the edges of the micro-magnet as simulated.



Supplementary Fig. S10. The same as in Fig. S9 when the external magnetic field is applied along the x' axis.



Supplementary Fig. S11. Effect of $\mathbf{B}_{\text{micro}}$ on the total homogeneous magnetic field. **A**, Anisotropic total magnetic field, due to the presence of the homogeneous magnetic field from the micro-magnet, $\mathbf{B}_{\text{micro}}^{\theta}$. $\mathbf{B}_{\text{micro}}^{\theta}$ adds vectorially to \mathbf{B}_{ext} . Also the magnetization of the micro-magnet depends on the direction of \mathbf{B}_{ext} or θ . So $\mathbf{B}_{\text{micro}}^{\theta}$ itself is anisotropic, hence the superscript θ . **B**, Total magnetic field (shown in green dashed line with square markers) along along $[110]$ ($\theta = 0^\circ$) (bottom panel) and $[\bar{1}\bar{1}0]$ ($\theta = 90^\circ$) (top panel) with changing B_{ext} . The black line represents $B_{\text{tot}} = B_{\text{ext}}$.

-
- [1] Veldhorst, M. *et al.* Spin-orbit coupling and operation of multivalley spin qubits. *Phys. Rev. B* **92**, 201401(R) (2015).
 - [2] Nestoklon, M. O., Ivchenko, E. L., Jancu, J. -M., & Voisin, P. Electric field effect on electron spin splitting in SiGe/Si quantum wells. *Phys. Rev. B* **77**, 155328 (2008).
 - [3] Nestoklon, M. O., Golub, L. E., & Ivchenko, E. L. Spin and valley-orbit splittings in SiGe/Si heterostructures. *Phys. Rev. B* **73**, 235334 (2006).
 - [4] Roth, L. g Factor and Donor Spin-Lattice Relaxation for Electrons in Germanium and Silicon. *Phys. Rev.* **118**, 1534 (1960)
 - [5] Goldman, J. R., Ladd, T. D., Yamaguchi, F., & Yamamoto, Y. Magnet designs for a crystal lattice quantum computer. *Appl. Phys. A* **71**, 11 (2000).
 - [6] Pioro-Ladrière, M., Tokura, Y., Obata, T., Kubo, T. & Tarucha, S. Micromagnets for coherent control of spin-charge qubit in lateral quantum dots. *Applied Physics Letters* **90**, 024105 (2007).
 - [7] Kawakami, E. *et al.* Electrical control of a long-lived spin qubit in a Si/SiGe quantum dot. *Nature Nanotechnology* **9**, 666670 (2014).